energies

MDPI

Article

Flow Induced Vibration and Energy Extraction of an Equilateral Triangle Prism at Different System Damping Ratios

Jun Zhang, Fang Liu, Jijian Lian *, Xiang Yan and Quanchao Ren

State Key Laboratory of Hydraulic Engineering Simulation and Safety, Tianjin University, Tianjin 300072, China; zhangjun5053@163.com (J.Z.); fangliu@tju.edu.cn (F.L.); xiangyan@tju.edu.cn (X.Y.); 2014205258@tju.edu.cn (Q.R.)

* Correspondence: tju_luntan@126.com; Tel.: +86-22-2740-1127

Academic Editor: Lieven Vandevelde

Received: 25 August 2016; Accepted: 3 November 2016; Published: 10 November 2016

Abstract: The flow induced vibration and energy extraction of an equilateral triangle prism elastically mounted in a water channel are investigated experimentally at different system damping ratios ζ_{total} with the constant oscillating mass M_{osc} and system stiffness K. A power take-off system with a variable damping function is developed. The translation-rotation equation of the vibration system deduced in the study indicates that the total oscillating mass includes the material mass, and the equivalent mass due to the rotation of the gears and rotor. Besides, increasing load resistance can result in a decrease in ζ_{total} when K and M_{osc} remain unchanged. The prism experiences, in turn, soft galloping, hard galloping 1 and hard galloping 2 with increasing ζ_{total}. As ζ_{total} increases up to 0.335, only the vortex-induced vibration is observed because the extremely high ζ_{total} prevents the prism from galloping. The response amplitude decreases with the increasing ζ_{total}. In addition, higher ζ_{total} promotes the galloping to start at a higher reduced velocity. The galloping characteristics of the prism, including large amplitude responses in an extremely large range of flow velocities, excellent vibration stationarity, and steady vibration frequencies, are beneficial for improving energy conversion. The prism can extract hydraulic energy for the flow velocity $U > 0.610$ m/s. The harnessed power P_{out} and the energy conversion efficiency η_{out} increase with increasing ζ_{total} in the galloping zone. The maximum P_{out} and η_{out} reach 53.56 W and 40.44%, respectively. The optimal system damping ratio for extracting energy is the maximum system damping ratio that the prism can overcome to experience stable galloping.

Keywords: equilateral triangle prism; flow induced vibration; damping ratio; vortex induced vibration; galloping; energy extraction

1. Introduction

Flow induced vibration (FIV) of a rigid cylinder on springs immersed in a steady transverse flow has been a subject of interest for the past several decades. An elastically mounted smooth circular cylinder can only undergo vortex-induced vibration (VIV) in isolated conditions [1–3], but non-circular sections (such as squares and triangles) can be subject to galloping [4–7].

VIV occurs due to the alternating shedding of vortices from either side of the bluff cylinder [1]. The alternating shedding of vortices gives rise to periodic changes in the pressure distribution on the cylinder surface, which indicates that the VIV of bodies is a self-excited motion. However, galloping, characterized by the large amplitude and low frequency oscillation normal to the flow, is caused by a coupling between the aerodynamic forces and the across-flow oscillation induced in the structure [8]. The periodically varying angle of attack results in periodic changes in the aerodynamic forces acting on the cylinder.

FIV is always treated as a destructive phenomenon in the civil engineering field because it can lead to the failure of the oscillating structure. Many researchers have devoted great efforts to the suppression of FIV. With an entirely opposite objective, in early studies [9,10]. Bernitsas and his colleagues developed the vortex induced vibration for aquatic clean energy (VIVACE) converter. The VIVACE unit, which captures the hydrokinetic energy in ocean currents or rivers utilizing the FIV of a cylinder or cylinder array, is an innovative energy harnessing device with a high energy density, low operable flow velocities and low maintenance cost. Besides, this device satisfies all of the requirements set by the California Energy Commission and the U.S. DOE [9]. In order to convert more hydrokinetic energy to mechanical energy and subsequently to electrical energy over broader velocity range, Chang et al. [11], Park et al. [12] and Ding [13] tried to enhance the FIV of the circular cylinder by altering the cylinder surface roughness with the help of Passive Turbulence Control (PTC). The maximum energy conversion efficiency was increased from 22% [10] to 28% [13].

Numerous publications have reported that flow around an elastically mounted circular cylinder can induce the periodic vibration of the cylinder in a certain range of flow velocities. However, non-circular section cylinders with symmetric sharp edges, such as rectangular section prisms as well as isosceles or equilateral triangular cylinders could be more susceptible to undergoing FIV because the symmetric apex angles on their surface appear to be helpful for the flow to separate from the body surface. Kluger [14] and Sorribes-Palmer et al. [15] explained the role of different dimensionless parameters in the determination of maximum energy extraction. In the last decades, the FIV of non-circular section bodies has received more and more attention from scientists. Most of the studies have concentrated on square or rectangular section bodies [16–22]. Nemes et al. [21] investigated the influence of the orientation of the square prism on FIV and found that the prism with a low mass ratio can undergo the combination of VIV and galloping in a narrow range of flow approaching angles. This phenomenon was also observed by Barrero–Gil and Fernandez–Arroyo [22]. In contrast to the research related to the flow past circular and rectangular section cylinders, there are limited studies that focus on a triangular cylinder immersed in a uniform flow because the triangular prism is seldom used in building structures. Several researchers have emphasized the influence of the wind direction and the cross-sectional shape on the flow past a triangular cylinder [23–26]. They demonstrated that the fluctuating cross-flow forces connected with the vortex shedding vary significantly with the incident flow orientation and the aspect ratio. Furthermore, Alonso et al. [27,28] comprehensively studied the transverse galloping stability of triangular prisms based on the Glauert-Den Hartog criterion and dynamical tests. They concluded that the stability to transverse galloping of triangular cross-section cylinders depends on the cross-sectional geometry and the angle of attack. In addition, Lin Ding et al. [6] investigated the FIV perpendicular to the flow of an equilateral triangular prism on springs by means of numerical calculations and indicated that the FIV of an elastically mounted equilateral triangular cylinder can be divided into the initial and upper branches of VIV, the transition branch from the VIV branch to the galloping branch, and the galloping branch, regarding the amplitude and frequency responses. Xu and Ou [7] also performed a numerical investigation of the FIV of elastically mounted cylinders with different sections and concluded that the FIV of the square and triangle prisms change from vortex induced vibration to galloping as the ratio of the natural frequency to the Strouhal frequency (the vortex shedding frequency of the fixed cylinder) decreases.

As indicated by previous researchers, the triangular prism on springs can also undergo strong FIV in an extremely broad range of flow velocities. The prism enters into galloping mode when the velocity of the incident flow increases beyond a threshold value, and its response amplitude increases with increasing flow velocities in the galloping branch. Consequently, the use of a triangular prism as an alternative oscillator to extract energy from a fluid flow has obvious advantages. However, as far as we know, almost all of the researches on the FIV of triangular prisms were investigated by means of wind tunnel tests [8,25–28] or numerical simulations [6,7,23,24]. There is a lack of experimental data concerning the characteristics and application of the FIV of elastically mounted

triangle cylinders immersed in the water flow. However, there are great differences between the dimensionless parameters (including M^*, A^*, U_r and ζ) in the air and water environments.

The objective of the present study was to examine the FIV characteristics of an equilateral triangle prism elastically mounted in water at high damping ratios as well as the effects of the damping ratio on the FIV and energy conversion. In Section 2, the experimental apparatus is described, and the translation-rotation equation of the vibration system is deduced. The results of free decay experiments are presented in Section 3. In Section 4, the results of FIV tests and the energy extraction are discussed. The conclusions are summarized at the end.

2. Experimental Apparatus and Mathematical Model

2.1. Water Channel

The experiments are performed in the recirculating water channel at the State Key Laboratory of Hydraulic Engineering Simulation and Safety of Tianjin University. The channel has a main test section of 1 m in width and 1.5 m in depth. The water in the channel is forced by an impeller powered by a 90 kW variable frequency motor, which provides flow velocities in the range from 0 to approximately 1.6 m/s, corresponding to Reynolds Numbers (Re = $U \cdot D/\nu$ where ν is the kinematic viscosity of water) ranging from 0 to 1.29×10^5.

2.2. Vibration System

Figure 1 shows the vibration system consisting of Parts 1–8 as identified and listed in Table 1. The test prism is mounted on side struts and constrained to move in the y direction (perpendicular to the flow direction) using linear bearings. The side struts are made of duralumin plate, and each side strut with dimensions of $1.51 \times 0.1 \times 0.006$ m is 1.616 kg in weight. The side struts, the power take-off system and the linear bearings are connected rigidly by the connection structure suspended by tension springs. Besides, the upper and the lower ends of the spring are fixed on the vertical points to keep the spring in vertical condition. The springs are always under tension in the test process.

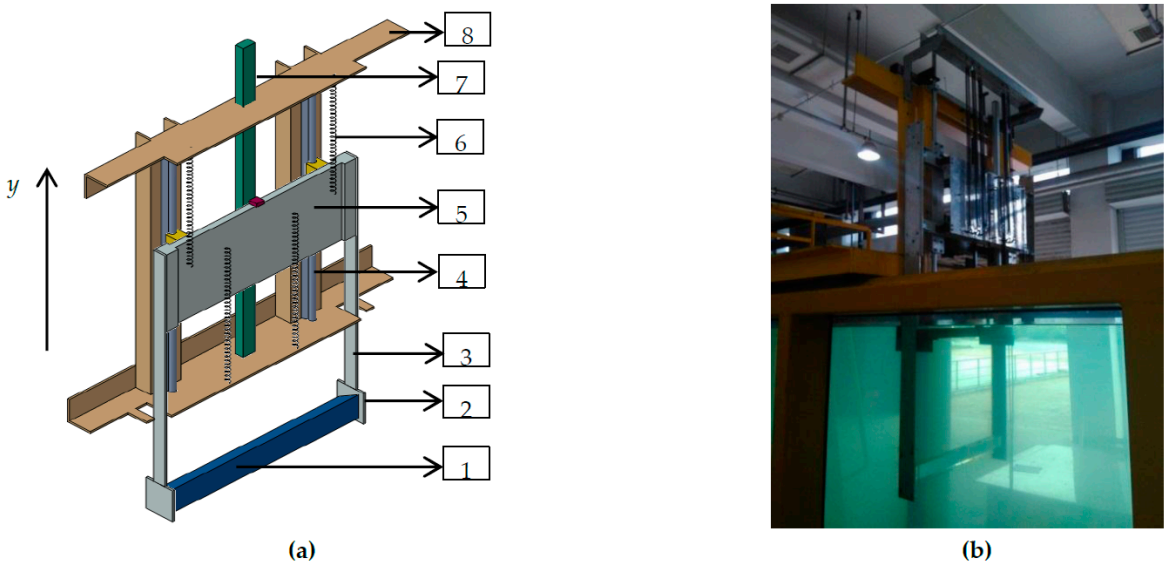

Figure 1. Vibration system with an equilateral triangle prism (**a**) Parts of vibration system; (**b**) Picture of vibration system.

The equilateral triangle prism in the present investigation is made of polymethyl methacrylate. Endplates with dimensions of $0.18 \times 0.11 \times 0.01$ m are attached on the both ends of the prism to induce parallel shedding at high Reynolds number tests [29–31], as shown in Figure 2a. The oscillator

is mounted on the side struts. A gap of 34 mm is maintained between the walls of the water channel and the side struts. The cross section of the equilateral triangular prism is 0.1 m in length. One of the side edges is placed facing the incident flow, as depicted in Figure 2b, because triangular cross-section prisms are prone to galloping instability when the base of the triangle is facing the flow [8]. The oscillator particulars are listed in Table 2. Note that the displaced fluid mass is defined as $m_d = \rho D^2 L\sqrt{3}/4$.

Table 1. Main components of the vibration system.

Part No.	Description
1	Equilateral triangle prism
2	Endplates
3	Side strut used for connecting the prism and connection structure
4	Linear bearings playing a role in limiting the system to vibration in the vertical direction
5	Connection structure used for connecting side struts, linear bearings and a power take-off system
6	Tension springs
7	Displacement transducer
8	Steel frame used for fixing linear bearings, tension springs, displacement transducer and generator

Table 2. Physical model parameters.

Side Length of the Cross Section D	Length of the Prism L	Aspect Ratio of the Prism $\alpha = L/D$	Displaced Fluid Mass m_d	Oscillating Material Mass m_{osc}
0.1 m	0.9 m	9	7.07 kg	30.04 kg

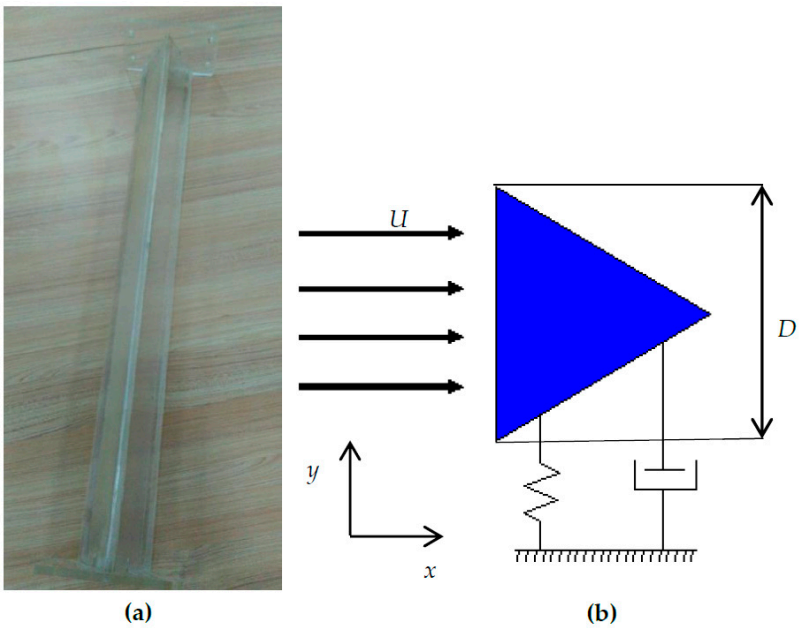

Figure 2. Oscillator (**a**) Equilateral triangle prism; (**b**) Installation way of the equilateral triangle prism in the channel.

The vertical displacement measurement is performed using a non-contact magnetic induction displacement transducer with a measuring range from 0 to 800 mm. The accuracy of the displacement transducer is within ±0.05%, giving a displacement measurement resolution of 0.001%FS. The flow velocity is measured using the Pitot tube with a differential pressure transmitter. The accuracy of the differential pressure transmitter is within ±0.1% of the 6 kPa linear range available, and its resolution

is within 0.01% FS. The voltage measurement is done by directly connecting the generator to the data acquisition system. All the data are recorded for a time interval of 30 s at a 50 Hz sampling rate.

2.3. Power Take-off System

When a generator runs, the wire loop cutting across the magnetic induction lines yields an induction current. However, the electromotive force due to the induction current always resists the relative motion between the stator and rotor. A power take-off system with the function of variable damping is developed depending on this principle, which is shown in Figure 3.

The power take-off system consists of a rack, three gears with different diameters, and a generator. The rack mounted on the connection structure meshing with Gear 1 converts the linear oscillatory mechanical motion of the prism in FIV to a rotational oscillatory motion of Gear 1. Gear 1 connects with Gear 2 via swivel bearings, and Gear 3 mounted on the generator shaft meshes with Gear 2. Gear 1, Gear 2 and Gear 3 constitute a variable speed system.

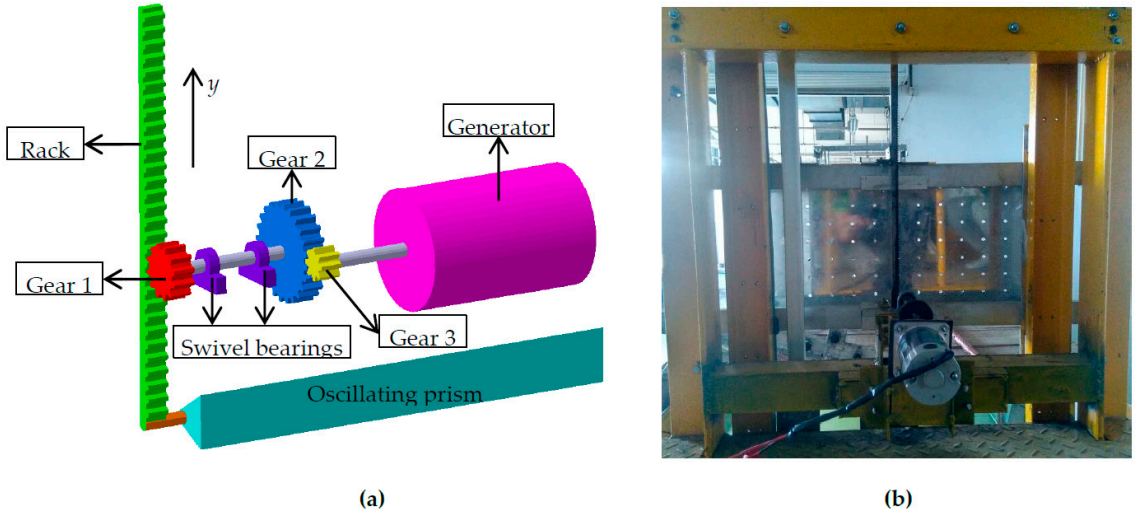

Figure 3. Power take-off system (**a**) Diagram of Power take-off system; (**b**) Mounting position.

Assuming that both shafts are rigid and that there is no slip in the transmission system, the rack is equal to Gear 1 in linear velocity due to the engagement between the rack and Gear 1, which is:

$$V_1 = \dot{y} \tag{1}$$

where V_i and $\dot{y}$ are linear velocities of Gear i and the rack (prism), respectively.

Gear 1 and Gear 2 revolve around the same shaft. Correspondingly, their angular velocities are equal:

$$\dot{\theta}_1 = \dot{\theta}_2 \tag{2}$$

where $\dot{\theta}_i$ denotes the angular velocity of Gear i.

The linear velocity of Gear i can be calculated by:

$$V_i = r_i \dot{\theta}_i \tag{3}$$

where r_i is the radius of Gear i.

Substituting Equations (3) into (2) yields:

$$\frac{V_1}{r_1} = \frac{V_2}{r_2} \tag{4}$$

From Equations (1) and (4), the linear velocity of Gear 2 can be expresses as:

$$V_2 = \frac{r_2}{r_1} V_1 = \frac{r_2}{r_1} \dot{y} \tag{5}$$

Due to the relation that Gear 3 meshes with Gear 2, the linear velocity of Gear 3 can be written as:

$$V_3 = V_2 = \frac{r_2}{r_1} \dot{y} \tag{6}$$

Gear 3 and the generator rotor revolving around the generator shaft yields:

$$\dot{\theta}_g = \dot{\theta}_3 = \frac{V_3}{r_3} = \frac{r_2}{r_1 r_3} \dot{y} \tag{7}$$

where $\dot{\theta}_g$ is the angular velocity of the generator rotor.

The linear velocity of the generator rotor is given by the following equation:

$$V_g = r_g \dot{\theta}_g = \frac{r_4 r_2}{r_1 r_3} \dot{y} \tag{8}$$

where V_g denotes the linear velocity of the generator rotor, and r_g is the radius of the generator rotor.

The induced voltage of the generator is defined as:

$$E = BlV_{\mathrm{g}} \tag{9}$$

where B is the magnetic flux density, and l is the length of the wire cutting the a magnetic field perpendicularly to the field lines.

The induced current is defined as:

$$I = \frac{E}{R_0 + R_L} \tag{10}$$

where R_0 denotes the inner resistance of the generator, and R_L is the external load resistance.

The electromotive force created by the relative movement of a circuit and a magnetic field is defined as:

$$F_{mag} = BIl \tag{11}$$

By substituting Equations (8)–(10) into (11), the electromotive force can be rewritten as:

$$F_{mag} = \frac{B^2 l^2}{R_0 + R_L} V_g = \frac{B^2 l^2}{R_0 + R_L} \times \frac{r_g r_2}{r_1 r_3} \dot{y} \tag{12}$$

The electromotive force torque of the generator T_{mag} is proportional to the rotor radius and the electromotive force, which is:

$$T_{mag} = r_g F_{mag} = \frac{B^2 l^2}{R_0 + R_L} \times \frac{r_g^2 r_2}{r_1 r_3} \dot{y} \tag{13}$$

The movement of the vibration system consists of the linear vibration of the oscillator and the rotational oscillatory motion of the power take-off system.

The rotational oscillatory motion equation of the generator is given by:

$$J_3 \ddot{\theta}_3 + r_3^2 c_3 \dot{\theta}_3 + J_g \ddot{\theta}_g + r_g^2 c_g \dot{\theta}_g = T_3 - T_{mag} \tag{14}$$

where J_i and J_g are respectively the rotational inertia of the ith wheel and the rotor, c_i and c_g are respectively the damping coefficients due to the frictional losses on the ith wheel and on the rotor, T_3 is

the torque on Gear 3 (supplied by Gear 2), $\ddot{\theta}_i$ and $\ddot{\theta}_g$ are respectively the angular acceleration of the ith wheel and the rotor.

The generator rotor and Gear 3 revolve around the same shaft. Thus:

$$\ddot{\theta}_3 = \ddot{\theta}_g \tag{15}$$

Due to Equations (7) and (15), Equation (14) becomes:

$$\left(J_3 + J_g\right)\ddot{\theta}_3 + \left(r_3^2 c_3 + r_g^2 c_g\right)\dot{\theta}_3 = T_3 - T_{mag} \tag{16}$$

The rotational oscillatory motion equation of Gear 1 and Gear 2 is given by the following equation (not taking into account the rotational inertia and the damping coefficient of the swivel bearings):

$$J_1\ddot{\theta}_1 + r_1^2 c_1\dot{\theta}_1 + J_2\ddot{\theta}_2 + r_2^2 c_2\dot{\theta}_2 = T_1 - T_2 \tag{17}$$

where T_1 is the torque supplied to Gear 1 induced by the linear motion of the prism in FIV, and T_2 is the torque transmitted to Gear 2.

In the same manner, the Equation (17) can be simplified as:

$$\left(J_1 + J_2\right)\ddot{\theta}_1 + \left(r_1^2 c_1 + r_2^2 c_2\right)\dot{\theta}_1 = T_1 - T_2 \tag{18}$$

Assuming that there is no energy loss in Gear 2 and Gear 3, their power is coincident:

$$T_2\dot{\theta}_2 = T_3\dot{\theta}_3 \tag{19}$$

Gear 2 is equal to Gear 3 in linear velocity due to the engagement:

$$r_2\dot{\theta}_2 = r_3\dot{\theta}_3 \tag{20}$$

Then:

$$T_2 = \frac{\dot{\theta}_3}{\dot{\theta}_2}T_3 = \frac{r_2}{r_3}T_3 \tag{21}$$

$$\ddot{\theta}_1 = \ddot{\theta}_2 = \frac{r_3}{r_2}\ddot{\theta}_3 \tag{22}$$

Substituting Equations (21) and (22) into (16) yields:

$$T_2 = \frac{r_2}{r_3}\left[\frac{r_2}{r_3}\left(J_3 + J_g\right)\ddot{\theta}_1 + \frac{r_2}{r_3}\left(r_3^2 c_3 + r_g^2 c_g\right)\dot{\theta}_1 + T_{mag}\right] \tag{23}$$

Substituting Equations (23) into (18) yields:

$$T_1 = \left[J_1 + J_2 + \left(\frac{r_2}{r_3}\right)^2\left(J_3 + J_g\right)\right]\ddot{\theta}_1 + \left[r_1^2 c_1 + r_2^2 c_2 + \left(\frac{r_2}{r_3}\right)^2\left(r_3^2 c_3 + r_g^2 c_g\right)\right]\dot{\theta}_1 + \frac{r_2}{r_3}T_{mag} \tag{24}$$

The force exerted on Gear 1 by the rack is given by:

$$F_1 = T_1/r_1 \tag{25}$$

As was assumed in [9], when the cylinder is in FIV, its motion can be approximated by the following linear equation:

$$m_{osc}\ddot{y} + c_{structure}\dot{y} + Ky = F_y \tag{26}$$

where m_{osc} denotes the material mass of the vibration system including the oscillator, side struts, the connection structure, endplates and 1/3 tension springs [9,10], y is the displacement perpendicular to the incident flow and the cylinder axis, $c_{structure}$ is the damping coefficient due to the frictional losses on the linear bearings, K is the system spring stiffness, F_y is the force exerted by the fluid on the body surface in the y-direction.

Considering the feedback force from Gear1 (equal to F_1), the linear equation can be rewritten as:

$$m_{osc}\ddot{y} + c_{structure}\dot{y} + Ky = F_y - F_1 \tag{27}$$

The angular acceleration of the prism can be expressed as:

$$\ddot{y} = r_1\ddot{\theta}_1 \tag{28}$$

and its linear velocity is given by:

$$\dot{y} = r_1\dot{\theta}_1 \tag{29}$$

Substituting the Equations (24), (25), (28) and (29) into (27) yields the translation-rotation equation of the vibration system, which is:

$$\begin{gathered}\left[m_{osc} + \frac{J_1+J_2}{r_1^2} + \left(\frac{r_2}{r_1 r_3}\right)^2 (J_3 + J_g)\right]\ddot{y} \\ + \left[c_{structure} + \frac{r_1^2 c_1 + r_2^2 c_2}{r_1^2} + \left(\frac{r_2}{r_1 r_3}\right)^2 \left(r_3^2 c_3 + r_g^2 c_g\right)\right]\dot{y} + \frac{r_2}{r_1 r_3} T_{mag} + Ky = F_y\end{gathered} \tag{30}$$

Based on Equation (13), Equation (30) can be rewritten as:

$$\begin{gathered}\left[m_{osc} + \frac{J_1+J_2}{r_1^2} + \left(\frac{r_2}{r_1 r_3}\right)^2 (J_3 + J_g)\right]\ddot{y} \\ + \left[c_{structure} + \frac{r_1^2 c_1 + r_2^2 c_2}{r_1^2} + \left(\frac{r_2}{r_1 r_3}\right)^2 \left(r_3^2 c_3 + r_g^2 c_g\right) + \left(\frac{r_g r_2}{r_1 r_3}\right)^2 \frac{B^2 l^2}{R_0 + R_L}\right]\dot{y} + Ky = F_y\end{gathered} \tag{31}$$

Equivalent mass due to the rotation of the gears and rotor is defined as:

$$m_{equ} = \frac{J_1 + J_2}{r_1^2} + \left(\frac{r_2}{r_1 r_3}\right)^2 (J_3 + J_g) \tag{32}$$

As shown in Equation (32), the equivalent mass is associated with the radius and the rotational inertia of the gears and rotor.

The total system damping coefficient c_{total} can be expressed as:

$$c_{total} = c_{structure} + c_{tra} + c_{gen} + c_{harn} \tag{33}$$

The transmission damping coefficient c_{tra} is due to friction in the gear system, the generator and bearings:

$$c_{tra} = \frac{r_1^2 c_1 + r_2^2 c_2}{r_1^2} + \left(\frac{r_2}{r_1 r_3}\right)^2 \left(r_3^2 c_3 + r_g^2 c_g\right) \tag{34}$$

The generator damping coefficient c_{gen} is due to the generator internal resistance R_0. c_{harn} is the damping coefficient due to the external load resistance R_L used to harness energy. Then:

$$c_{gen} + c_{harn} = \left(\frac{r_g r_2}{r_1 r_3}\right)^2 \frac{B^2 l^2}{R_0 + R_L} = \lambda \frac{1}{R_0 + R_L} \tag{35}$$

where λ is defined as the deceleration coefficient associated with the radius of the gears and rotor, which is:

$$\lambda = \left(Bl \frac{r_g r_2}{r_1 r_3} \right)^2 \tag{36}$$

The generator damping coefficient due to the generator internal resistance is a function of the load resistance. The equivalent mass m_{equ} and the deceleration coefficient λ can be chosen to verify the translation-rotation equation indirectly, which will be shown in Section 3.

Thus, Equation (31) can be rewritten as:

$$\left(m_{osc} + m_{equ}\right) \ddot{y} + \left(c_{structure} + c_{tra} + c_{gen} + c_{harn}\right) \dot{y} + Ky = F_y \tag{37}$$

As shown in Equation (37), the total oscillating mass of the vibration system M_{osc} includes the material mass m_{osc}, and the equivalent mass m_{equ} due to the rotation of the gears and rotor. Thus, the mass ratio of the vibration system can be defined as:

$$M^* = \frac{M_{osc}}{m_d} \tag{38}$$

For a given permanent magnet generator, the parameters including the magnetic flux density B, the length of the wire loop L, the rotor radius r_g and the generator internal resistance R_0 are constants. The variation of the deceleration coefficient λ and the load resistance R_L can change the total damping coefficient c_{total} thus varying the total damping ratio $\zeta_{total} = c_{total}/2\sqrt{M_{osc}K}$, as revealed in Equation (35). However, to examine the effects of the system damping ratio ζ_{total} on the FIV and energy conversion of an equilateral triangle prism in water, the system stiffness and the total oscillating mass should remain unchanged when the ζ_{total} varies. Thus, the variation of the total damping ratio is implemented by adjusting the load resistance R_L in the present study.

3. Free Decay Damping Experiment

The purpose of free decay damping experiments is to verify the translation-rotation equation deduced in the present investigation and to obtain the total system damping ratio and the natural frequency of the vibration system with different load resistance R_L. The high-power resistors with different resistance are chosen in the present study, which are shown in Figure 4. The maximum and minimum resistance values of resistors are 50 Ω and 1 Ω, respectively. The variation of R_L is conducted by the parallel and series connection of resistors. All the damping tests are performed at K = 1228 N/m.

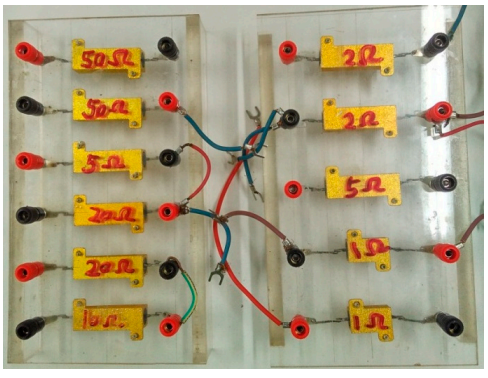

Figure 4. High-power resistors with different resistance.

The equivalent mass m_{equ} and the deceleration coefficient λ can't be obtained depending on Equations (32) and (36) because the generator used in the present research does not provide the rotor radius r_g, the magnetic flux density B, and the length of the wire loop l. However, m_{equ} and λ can be

judged to be constants because, for a given vibration system with a permanent magnet generator, the parameters of the gears including r_i and J_i as well as the generator parameters including B, l, J_g and r_g are constants. Accordingly, m_{equ} and λ calculated by the results of free decay damping test can be used to validate the translation-rotation equation.

Free decay damping experiments with different R_L are conducted in air. R_L ranges from 5.39 to 51.37 Ω. For each R_L case, free decay tests are carried out four times, and the results are determined using a simple averaging method.

The damping ratio ζ_{total} can be determined using the logarithmic decrement method depending on the test results, which can be expressed as:

$$\zeta_{total} = \frac{\ln\eta}{2\pi} = \frac{1}{2\pi}\ln(\frac{A_i}{A_{i+1}}) \tag{39}$$

where A_i is the amplitude of the ith peak.

The natural frequency of the vibration system is extracted using FFT for the time histories of the displacement of free decay experiment.

In addition, the natural frequency of the vibration system can be expressed as:

$$f_{n,air} = \frac{1}{2\pi}\sqrt{\frac{K}{M_{osc}}} \tag{40}$$

The system damping ratio ζ_{total} is given by:

$$\zeta_{total} = \frac{c_{total}}{2\sqrt{M_{osc}K}} \tag{41}$$

The free decay experiments conducted in air can determine the damping ratio of the vibration system ζ_{total} as well as the natural frequency of the vibration system in air $f_{n,air}$. Substituting K and $f_{n,air}$ into Equation (40) can yield the total oscillating mass M_{osc} thus resulting in the equivalent mass $m_{equ} = M_{osc} - m_{osc}$. The system damping coefficient c_{total} can be calculated by substituting ζ_{total}, M_{osc} and K into Equation (41). For the open circuit (O/C) case where the load resistance R_L goes to infinity, the electrical losses due to the inner resistance are zero. Consequently, the damping tests performed in air for the open circuit case provides data to calculate the sum of $c_{structure}$ due to the frictional losses on the linear bearings plus c_{tra} due to friction in the gear system. The tests conducted for the closed circuit case provides data to calculate c_{total}.

The measured value of the generator inner resistance R_0 is 2.1 Ω. The equivalent mass m_{equ}, the deceleration coefficient λ and the system damping ratio ζ_{total} versus the load resistance R_L are plotted in Figures 5–7, respectively. The experiment results are listed in Table 3.

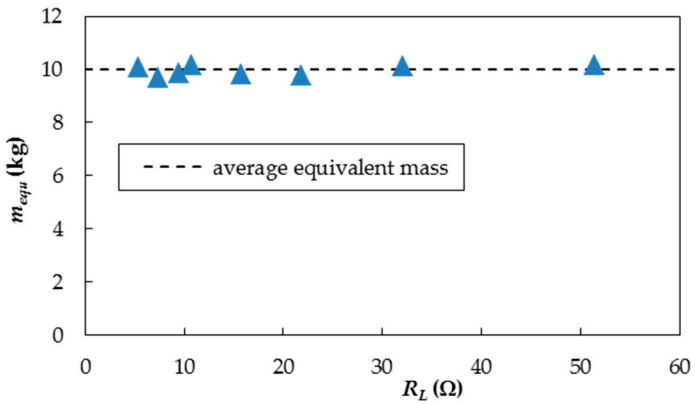

Figure 5. Equivalent mass m_{equ} versus load resistance R_L.

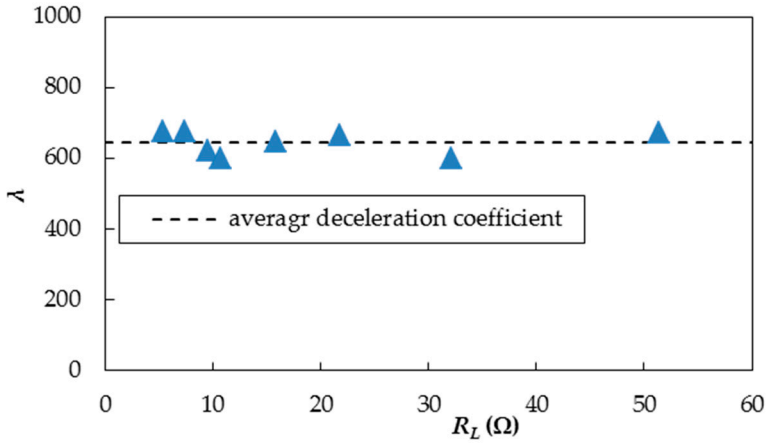

Figure 6. Deceleration coefficient λ versus load resistance R_L.

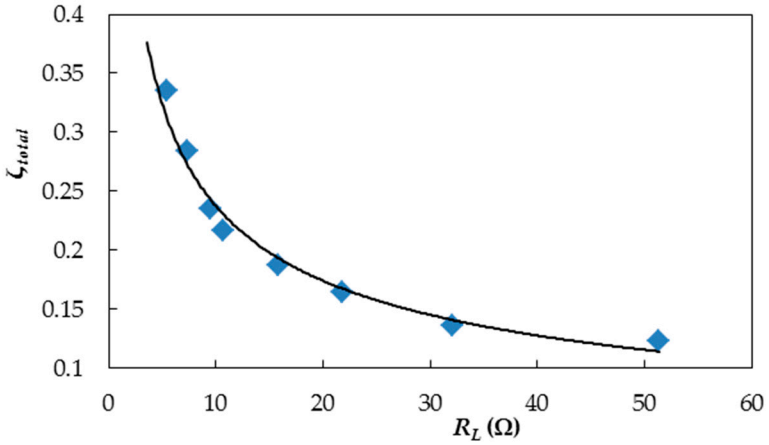

Figure 7. Damping ratio of the vibration system ζ_{total} versus load resistance R_L.

As shown in Figures 5 and 6, the equivalent mass m_{equ} and the deceleration coefficient λ remain approximately unchanged as the load resistance R_L ranges from 5.39 to 51.37 Ω. The maximum relative errors of m_{equ} and λ are respectively 3.2% and 7% indicating the translation-rotation equation derived in the present investigation is reasonable.

As presented in Figure 7, the damping ratio of the vibration system ζ_{total} decreases with the increasing load resistance R_L, which indicates that adjusting R_L can change the system damping ratio while the system stiffness K and the total oscillating mass M_{osc} remain unchanged. This is of great importance for examining the effects of the damping ratio on the FIV and energy conversion of a cylinder on springs.

Table 3. Free decay test results.

R_L (Ω)	ζ_{total}	$f_{n,air}$ (Hz)	c_{total} (N·s·m^{-1})	c_{gen} + c_{harn} (N·s·m^{-1})	M_{osc} (kg)
5.39	0.335	1.042	122.759	90.351	27.366
7.33	0.284	1.049	104.012	71.604	26.983
9.48	0.235	1.045	85.915	53.507	27.164
10.7	0.216	1.042	79.200	46.792	27.441
15.81	0.187	1.052	68.464	36.056	27.111
21.82	0.164	1.056	60.199	27.791	27.072
32.05	0.136	1.056	49.959	17.551	27.394
51.37	0.123	1.056	44.960	12.552	27.457
∞ (O/C)	0.089	1.058	32.408	0	27.583

The average of the total oscillating mass listed in Table 3, $M_{avg,osc}$ = 27.286 kg, is selected to calculate the total mass ratio of the vibration system, yielding $M^* = M_{avg,osc}/m_d$ = 6.36. Besides, the average of the nature frequency is adopted to obtain the reduced velocity and the response frequency ratio.

4. Results and Discussion

To examine the FIV characteristics and the energy conversion of an equilateral triangle cylinder on springs in water, a series of FIV experiments for the prism with nine sets of system damping ratios are carried out at K = 1228 N/m based on the power take-off system with the function of variable damping. All the experiments are performed at increasing the flow speed. The FIV response of the prism, which is influenced by extensive vibration system parameters, such as mass, stiffness and damping, has a large impact on the energy extraction. The present investigation focuses on the characteristics of the FIV of the prism at high damping ratio and on the effects of the damping ratio on the FIV and energy output. The system damping ratios ζ_{total} used in the FIV tests are listed in Table 3. In the present study, the reduced velocity U_r is introduced, which is defined as:

$$U_r = U/(f_{n,air}D) \tag{42}$$

where U is the flow velocity. The reduced velocity U_r is often used as the x-axis on plots in investigations on the FIV of a circle cylinder because the expression of experimental results in dimensionless form help to reduce the number of parameters and therefore to collapse many test cases into the same plot.

4.1. Amplitude and Frequency Responses

The maximum amplitude ratio $A^* = A/D$ and the frequency ratio $f^* = f_{osc}/f_{n,air}$ versus reduced velocity U_r along with the corresponding fluid velocity U and the Reynolds number Re for all ζ_{total} cases are plotted in Figure 8a,b, respectively. The maximum amplitude ratio $A^* = A/D$ is the average of all the peaks of oscillation over 30 s, and the response frequency of the prism is extracted using FFT for the time histories of displacement. Note that dashed lines in Figure 8 denote prism response with hard excitation where an externally initial threshold amplitude is imposed.

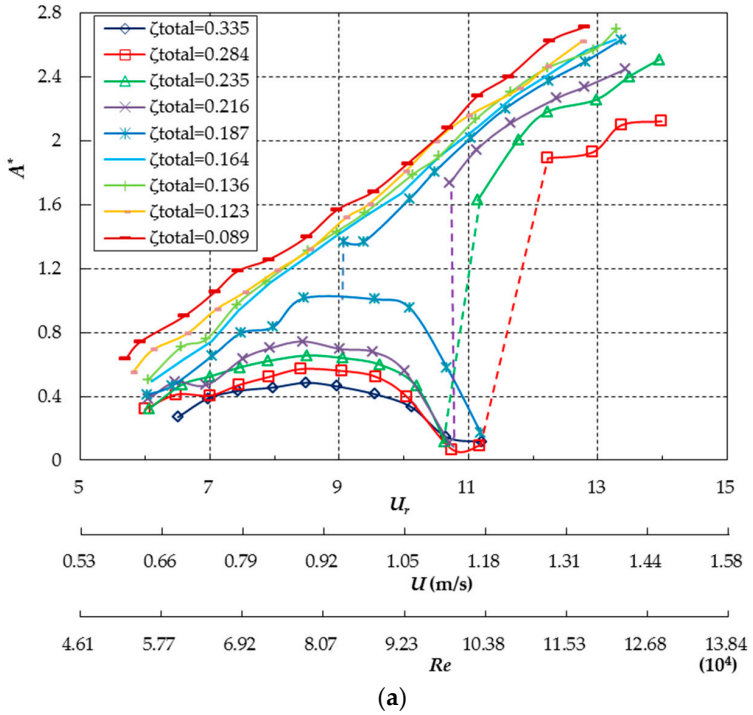

(**a**)

Figure 8. *Cont.*

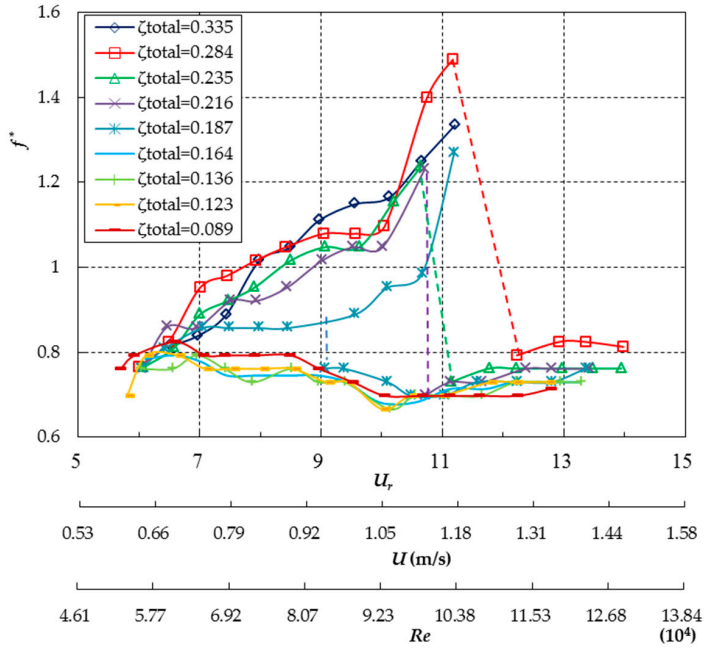

(**b**)

Figure 8. Amplitude and frequency (**a**) Amplitude ratio A^* versus U_r, U and Re for different ζ_{total}; (**b**) Frequency ratio f^* versus U_r, U and Re for different ζ_{total}; (Dashed lines denote hard excitation).

Figure 8 shows that the maximum amplitude ratio A^* is reduced with increasing ζ_{total}. This is expected as the mechanical energy in the vibration system, which is extracted from the hydrokinetic energy of the fluid flow, is dissipated more with higher ζ_{total} [15]. Besides, the galloping of the prism presents, in turn, the soft galloping (SG), the hard galloping 1 (HG1), and the hard galloping 2 (HG2) with increasing ζ_{total}. Soft galloping is defined as the self-initiated galloping, while hard galloping requires an externally imposed initial threshold amplitude [12]. The amplitude and frequency characteristics of the equilateral triangle prism for each ζ_{total} are summarized as follows:

1. SG. For $\zeta_{total} \leq 0.164$, A^* monotonically increases with increasing U_r, and f^* is less than 1 throughout the test U_r range revealing that the oscillation frequency is lower than the natural frequency of the vibration system in air. The FIV of the prism can be divided into four regions based on the amplitude and frequency responses: the vortex induced vibration (VIV) initial branch, the VIV upper branch, the transition branch from VIV to galloping, and the galloping branch. The transition from VIV to galloping is self-initiated, indicating the prism experiences SG. This is probably due to the fact that the amplitude in the VIV upper branch is high enough to induce galloping. In the VIV initial branch, f^* increases with increasing U_r accompanied with a low A^*. When the prism enter into the VIV upper branch, f^* firstly decreases and then levels off at approximately 0.729 to 0.793. The VIV of the prism is driven by the imposed lift on the body from vortex shedding [1]. In the transition branch from VIV to galloping, f^* declines sharply due to the coexistence of the driving mechanisms of oscillatory lift due to vortex shedding and instability inducing oscillatory lift due to shear layer motion in this transition region [6,11,12,21,22], and A^*continues to increase with increasing U_r. As the prism response is in galloping branch, f^* levels off at low values, and A^* still exhibits an increasing trend. The maximum A^* reaches 2.71 at U_r = 12.80 for ζ_{total} = 0.089. Note that A^* = 2.71 is the maximum value limited by the conditions in present experiments. In addition, the maximum A^* = 2.71 for the equilateral triangular prism exceeds the maximum A^* = 1.90 for a single circular cylinder reported by Raghavan and Bernitsas [32]. Galloping oscillation of the prism is mainly driven by lift instability, while the effect of vortex shedding on the motion in this region is negligible [6].

The reduced velocity U_r along with the corresponding fluid velocity U and Reynolds number Re for the onsets of the upper, lower and transition branches are listed in Table 4. The results show that higher ζ_{total} promotes the oscillation response mode to change at higher U_r, U and Re for $\zeta_{total} \leq 0.164$.

2. HG1. For the case $\zeta_{total} = 0.187$, without a given threshold initial displacement, the prism can only experience VIV, which is consistent with the response of a smooth circular cylinder consisting of an initial branch followed by an upper branch and ending in desynchronization branch [32]. At reduced velocity in the range of $6.03 \leq U_r \leq 7.04$, the amplitude ratio A^* and the frequency ratio f^* are small and increase rapidly with U_r indicating the oscillation response of the prism is in the VIV initial branch. For the reduced velocity U_r ranging from 7.04 to 10.09, A^* displays a more gradually increase firstly and then levels off with U_r accompanied with an approximately constant in f^*, which indicate the prism goes into the VIV upper branch. The VIV of the prism is suppressed significantly at $U_r > 10.09$ where A^* declines rapidly with increasing U_r while f^* continues to increase. The oscillation response of the prism is in the VIV desynchronization branch where f^* is more than 1 indicating the response frequency of the prism is higher than the nature frequency of the vibration system in air. When the prism is given a threshold initial displacement of approximately $1.5D$ at $U_r = 9.07$, the prism enters into HG1 where the oscillation response jumps to the galloping branch from the VIV upper branch [12]. This threshold amplitude is given to the prism by manually pushing the prism. For an initial displacement of less than $1.5D$, galloping was not initiated. In the HG1 branch, as shown in Figure 8, A^* continues to increase with increasing U_r while f^* remains around 0.75.
3. HG2. For the cases of $0.216 \leq \zeta_{total} \leq 0.284$, the prism only undergoes VIV without an externally imposed initial threshold amplitude. And the VIV characteristics are consistent with the case of $\zeta_{total} = 0.187$ except that f^* in VIV upper branch for the cases of $0.216 \leq \zeta_{total} \leq 0.284$ increase with increasing U_r while f^* exhibits lock-in for the case of $\zeta_{total} = 0.187$. After the VIV of the prism is strongly suppressed, a given threshold initial displacement of approximately $1.5D$ can excite the prism to gallop. The prism experiences HG2 because the VIV and galloping regions are separated by almost complete suppression [12]. In the HG2 branch, A^* monotonically increases with increasing U_r while f^* levels off into approximately 0.73~0.82. Besides, Figure 8 presents that the U_r where galloping is initiated increases as ζ_{total} increases in all galloping modes including SG, HG1 and HG2.
4. VIV. As ζ_{total} increases up to 0.335, only VIV is observed in the test velocity range ($U_r = 15.22$, $U = 1.6$ m/s). The response characteristics of A^* and f^* are consistent with those for the cases of $0.216 \leq \zeta_{total} \leq 0.284$ in the VIV modes.

Table 4. U_r, U and Re for onsets of the upper, lower and transition branches.

ζ_{total}	Onset of VIV Upper Branch			Onset of Transition Branch			Onset of Galloping Branch		
	U_r	U (m/s)	Re	U_r	U (m/s)	Re	U_r	U (m/s)	Re
0.089	6.60	0.694	60935	8.49	0.893	78386	10.06	1.057	92786
0.123	6.63	0.697	61215	8.54	0.897	78776	10.47	1.101	96643
0.136	6.65	0.730	64122	9.39	0.987	86662	10.54	1.108	97295
0.164	7.03	0.739	64857	9.45	0.990	86956	11.13	1.170	102709

In this section, an amplitude variation coefficient CV_A is introduced to quantitatively describe vibration stationarity [33], which is defined as:

$$CV_A = \frac{\sigma_A}{\overline{A}} = \frac{\sqrt{\frac{1}{N}\sum_{i=1}^{N}\left(A_i - \overline{A}\right)^2}}{\overline{A}} \tag{43}$$

where σ_A denotes the standard deviation of peak amplitudes, $\overline{A}$ is the average of peak amplitudes, N is the number of peak amplitudes, and A_i is the amplitude of the ith peak.

Stationarity of the FIV of the prism is an important property that describes the prism dynamics. Besides, excellent vibration stationarity of FIV is beneficial for an oscillator to extract energy from a fluid flow. Vibration stationarity can be represented as the variation of peaks of the displacement time history in a certain period where the flow velocity is constant. The physical interpretation of CV_A is that higher CV_A signifies poorer vibration stationarity. The CV_A versus the reduced velocity U_r, the fluid velocity U, and the Reynolds number Re for all ζ_{total} cases are presented in Figure 9.

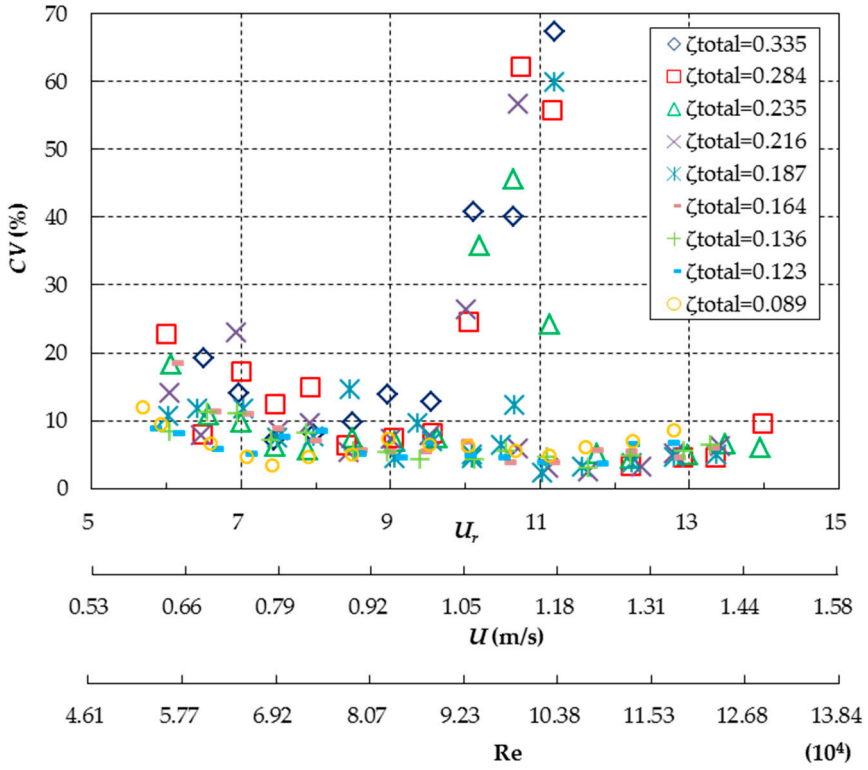

Figure 9. Amplitude variation coefficient CV_A versus U_r, U and Re for different ζ_{total}.

As shown in Figure 9, the CV_A versus the reduced velocity U_r for each ζ_{total} case is approximately coincident in VIV regions. In the VIV initial branch, the CV_A is relatively high and decrease with increasing U_r, which indicate that the vibration stationarity of the prism in the VIV initial branch is poor and increasing U_r can improve the vibration stationarity. As the prism enters into the VIV upper branch, the CV_A is lower and exhibits an approximately constant trend signifying the oscillation in the VIV upper branch is steady. The CV_A in the VIV desynchronization branch is high indicating the poor vibration stationarity in this branch. When the prism response exceeds the VIV regions, there exists inconsistency in CV_A versus U_r for different ζ_{total}. For $\zeta_{total} \leq 0.164$, the prism experiences SG where the transition from VIV to galloping is self-initiated and the VIV desynchronization branch is absent. The CV_A in the transition branch from VIV to galloping firstly increases and then decreases rapidly with increasing U_r. This behavior indicates that the amplitude modulation in the transition branch is severe, and the modulation is a manifestation of the transition from VIV to galloping. The CV_A levels off at low values in galloping branch indicating the prism maintains steady oscillation in fully developed galloping branch. For the cases of $0.187 \leq \zeta_{total} \leq 0.284$, the prism undergoes HG which is excited by an externally imposed initial threshold amplitude. The CV_A levels off at low values when the prism response is in galloping branch signifying that the prism experience the FIV with excellent stationarity in galloping branch.

4.2. Energy Extraction

The FIV test results indicate that an equilateral triangle prism elastically mounted in a water flow can maintain a significant FIV response at high damping ratio over an extremely broad velocity range. Contrary to a smooth circular cylinder which experiences significant oscillation with limited oscillation amplitudes in a narrow range of flow velocity, the galloping of an equilateral triangle prism develops in an infinite range of flow velocity without a self-limited response beyond the critical flow velocity. This behavior is clearly beneficial for an oscillator to convert energy from a fluid flow. Besides, the approximately constant response frequency, along with the excellent vibration stationarity of the prism in galloping region can significantly improve the electricity quality.

This section presents the comparison of the energy conversion of the prism at different system damping ratios. According to the output voltage, the harnessed power and the energy conversion efficiency, which can describe the performance of energy extraction of an equilateral triangle prism directly, are calculated by the following equations. The instantaneous power extracted via the oscillating prism is given by:

$$P_i = \frac{u_i^2}{R_L} \tag{44}$$

where u_i denotes the instantaneous voltage measured by directly connecting the generator to the data acquisition system, and R_L is the load resistance.

Correspondingly, the integrated power during an oscillation cycle of the prism is:

$$P_{out} = \frac{1}{T}\int_0^T P_i dt = \frac{1}{T}\int_0^T \frac{u_i^2}{R_L} dt \tag{45}$$

The energy conversion efficiency is defined as:

$$\eta_{out} = \frac{P_{out}}{P_w} = \frac{P_{out}}{(0.5\rho U^3 DL)} \tag{46}$$

where P_w is the total power in the fluid. In the present research, the characteristic width of the prism is adopted to calculate the total fluid power for the purpose of comparing the energy conversion efficiencies for an equilateral triangle prism with the efficiencies for circular cylinders reported by the research group of Bernitsas [9,10,13] who have compared the VIVACE with other energy conversion device. In addition, for an oscillating prism, the projected area where the prism encounters the fluid is $(2A + D)L$, but this projected area would not completely represent the utilized fluid power. Because the fluid in this area does not encounter the oscillating prism for the whole oscillating period, it is the projected area of DL that always encounters the flowing fluid by the prism [6,9].

The time histories of the measured instantaneous voltage along with the corresponding frequency spectra for ζ_{total} = 0.284 at U_r = 12.23 (the onset of the galloping) and at U_r = 13.98 (the maximum reduced velocity) are presented in Figures 10 and 11, respectively. As shown in Figures 10 and 11, the peaks for the output voltage fluctuate in a tight range and the dominant frequency is obvious in galloping branch due to the excellent vibration stationarity and the steady vibration frequency, which indicate that the equilateral triangle prism can convert the hydrokinetic energy to high quality electric energy. In addition, the spectra in the galloping branch present small peaks (probably due to vortex shedding) at the second and third harmonic components of the output voltage frequency (oscillation frequency), which implies that the frequency of the vortex shedding is much higher than the oscillation dominant frequency of the prism.

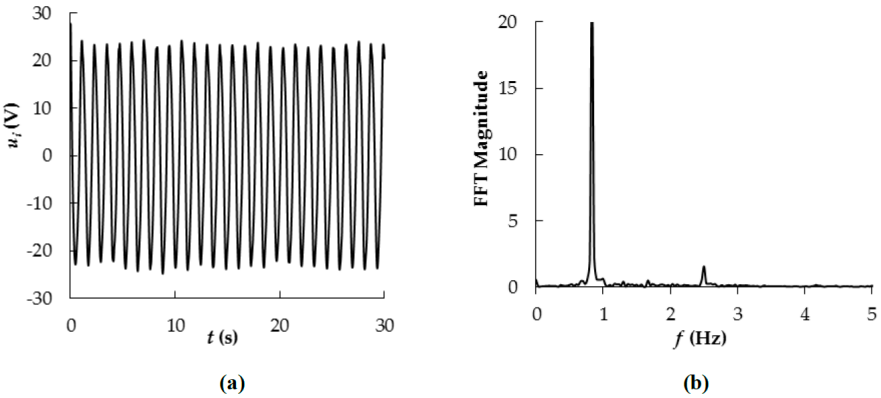

Figure 10. Voltage time histories and frequency spectra for ζ_{total} = 0.284 at U_r = 12.23 (**a**) Instantaneous voltage; (**b**) Frequency spectrum.

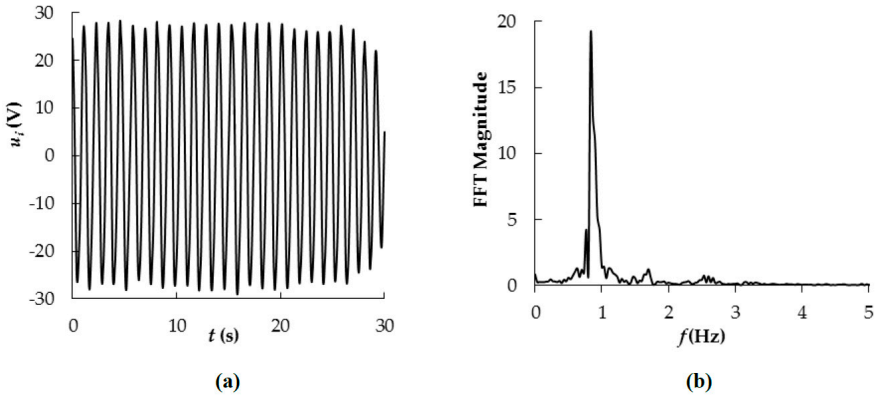

Figure 11. Voltage time histories and frequency spectrum for ζ_{total} = 0.284 at U_r = 13.98 (**a**) Instantaneous voltage; (**b**) Frequency spectrum.

Time histories of the instantaneous voltage u_i over 30 s are used to obtain the averaged value of P_{out}. The integrated power P_{out} versus the reduced velocity U_r, the fluid velocity U, and the Reynolds number Re is presented in Figure 12, which shows that the prism can extract hydraulic energy for $U_r > 5.80$, corresponding to $U > 0.610$ m/s and Re $> 5.36 \times 10^4$. The integrated power P_{out} for each ζ_{total} case in VIV regions especially in the VIV initial branch and the VIV desynchronization branch is small due to the low amplitude and frequency responses. When the prism enters into galloping, P_{out} increases with increasing ζ_{total} until ζ_{total} increases up to 0.335 where the galloping of the prism is completely suppressed. The maximum P_{out} of 53.56 W is achieved at U_r = 13.98 (U = 1.470 m/s, Re = 1.28×10^5) for the case of ζ_{total} = 0.284 in the present investigation. The harnessed power for ζ_{total} = 0.089 goes to zero due to R_L of infinity for the open circuit case. P_{out} for other ζ_{total} cases are summarized as follows:

1. For $0.089 < \zeta_{total} \leq 0.164$, the prism experiences SG where the transition from VIV to galloping is self-initiated and the VIV desynchronization branch is absent. P_{out} monotonically increases with U_r throughout the range of test water velocities thus yielding the peak P_{out} at the maxmum U_r. Besides, P_{out} increases with increasing ζ_{total} in all FIV branches.
2. For the case of $0.187 \leq \zeta_{total} \leq 0.284$, the prism undergoes HG excited by a given threshold initial displacement. P_{out} increases with increasing U_r in the VIV initial and upper branches while it is reduced with U_r when the prism goes in to the VIV desynchronization branch. Besides, higher ζ_{total} yields more harnessed power in the galloping branch.

3. As ζ_{total} increases up to 0.335, the prism can only experience VIV because the system damping ratio is high enough to prevent the prism from galloping. P_{out} versus U_r in the VIV regions is similar to that for the case of $0.187 \leq \zeta_{total} \leq 0.284$.

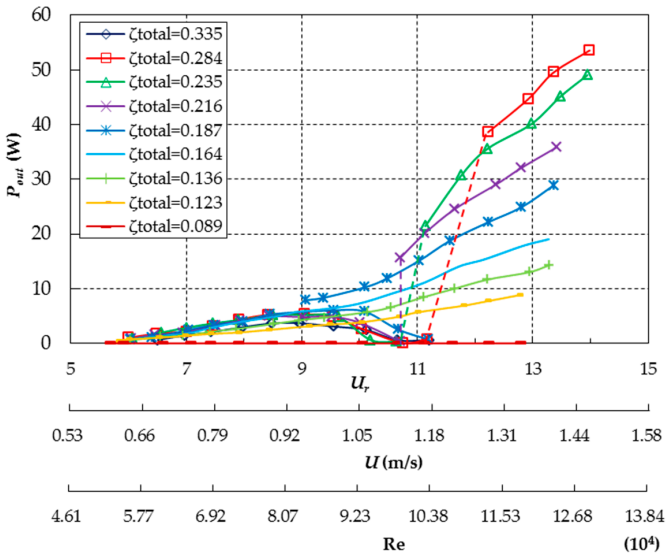

Figure 12. Harnessed power for different ζ_{system} (Dashed lines denote hard excitation).

In order to evaluate the optimum system damping ratio ζ_{total} to extract hydrokinetic energy from the fluid via the FIV of an equilateral triangle prism, the energy conversion efficiencies η_{out} of the FIV for the prism with different ζ_{total} are calculated by Equation (46). The comparison of the energy conversion efficiency is plotted in Figure 13.

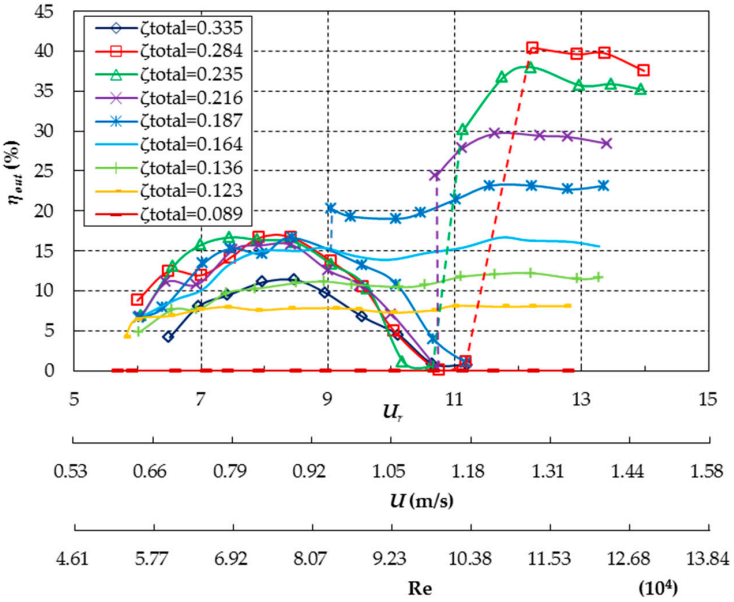

Figure 13. Efficiencies of the energy conversion for different ζ_{system} (Dashed lines denote hard excitation).

When the prism experiences SG for ζ_{total} in the range from 0.123 to 0.164, η_{out} increases with increasing ζ_{total} in all FIV branches. Besides, η_{out} increases rapidly with increasing U_r in the VIV

regions and then approximately levels off in the transition and galloping branches. For the cases of $0.187 \leq \zeta_{total} \leq 0.284$ where the prism undergoes HG, consistent with P_{out} shown in Figure 12, the energy conversion efficiency η_{out} presents an increasing trend with U_r in the VIV initial and upper branches and a decreasing trend in the VIV desynchronization branch. η_{out} versus U_r in the VIV regions nearly collapse. However, when the prism goes into the HG, visible differences of η_{out} for the different ζ_{total} are exhibited, as shown in Figure 13. η_{out} in galloping zone, including SG and HG, increases with increasing ζ_{total}. The maximum η_{out} of 40.44% is achieved for the case of $\zeta_{total} = 0.284$ at $U_r = 12.23$ ($U = 1.285$ m/s, Re = 1.12×10^5) where the HG1 is initiated. The η_{out} of the prism exceeds the efficiencies of the smooth circular cylinder ($\eta_{out} = 22\%$) [10] and the PTC circular cylinder ($\eta_{out} = 28\%$) [13].

As expected, an optimal value of system damping ratio for extracting hydrokinetic energy exists, which allows maximum energy extracting while maintaining FIV under high damping. For the vibration system in the present investigation, the optimal system damping ratio is 0.284. According to the results of the harnessed power and the energy extraction efficiency, it can be concluded that the optimal system damping ratio for extracting energy is the maximum system damping ratio that the prism can overcome to experience stable galloping.

5. Conclusions

The flow induced vibration and energy extraction of an equilateral triangle prism elastically mounted in a water channel were studied experimentally at a mass ratio $M^* = 6.36$ and system stiffness $K = 1228$ N/m for the system damping ratios varying from 0.089 to 0.335. A power take-off system with the function of variable damping was developed. In addition, the translation-rotation equation of the vibration system was deduced, which was verified by the free decay damping experiments. The responses of amplitude and frequency of the prism were discussed in the paper, along with the harnessed power and the energy conversion efficiency of the oscillating prism. The following conclusions can be drawn from the results presented in this paper:

1. The total oscillating mass of the vibration system includes the material mass m_{osc}, and the equivalent mass m_{equ} due to the rotation of the gears and rotor. Increasing load resistance R_L can result in a decrease in the system damping coefficient thus decreasing the system damping ratio when the system stiffness and the total oscillating mass remain unchanged.
2. The galloping of the prism presents, in turn, the soft galloping (SG), the hard galloping 1 (HG1) and the hard galloping 2 (HG2) with increasing ζ_{total}. For $\zeta_{total} \leq 0.164$, the prism experiences SG where the transition from VIV to galloping is self-initiated. The FIV of the prism can be divided into four regions: the VIV initial and upper branches, the transition branch from VIV to galloping, and the galloping branch. For the case of $\zeta_{total} = 0.187$, the prism only experiences VIV without an externally imposed initial threshold amplitude. The response of the prism consists of an initial branch followed by an upper branch and ending in a desynchronization branch. When the prism is given a threshold initial displacement of approximately $1.5D$ at $U_r = 9.07$, the prism enters into HG1 from the VIV upper branch. For the cases of $0.216 \leq \zeta_{total} \leq 0.284$, after the VIV of the prism is strongly suppressed, a given threshold initial displacement of approximately $1.5D$ can excite the prism to HG2. Higher ζ_{total} promotes the galloping to start at higher U_r, U and Re. In addition, as ζ_{total} increases up to 0.335, only VIV is observed in the test velocity range. For all ζ_{total} cases, A^* decreases with increasing ζ_{total}, and the maximum A^* reaches 2.71 at $U_r = 12.80$ for $\zeta_{total} = 0.089$.
3. The galloping characteristics of the equilateral triangle cylinder, including significant amplitude responses in an extremely large range of flow velocities, the excellent vibration stationarity, and steady vibration frequencies, are beneficial for improving energy conversion.
4. The prism can extract hydraulic energy for $U_r > 5.80$ ($U > 0.610$ m/s, Re $> 5.36 \times 10^4$). The harnessed power P_{out} and the energy conversion efficiency η_{out} increase with increasing

ζ_{system} in the galloping zone. The maximum P_{out} and η_{out} reach 53.56 W and 40.44%, respectively. In addition, the η_{out} of the prism exceeds the efficiencies of the smooth circular cylinder and the PTC circular cylinder. The optimal system damping ratio for extracting energy is the maximum system damping ratio that the prism can overcome to experience stable galloping.

Acknowledgments: This work is supported by the National Key Research and Development Program of China (Grant No. 2016YFC0401905). All workers from the State Key Laboratory of Hydraulic Engineering Simulation and Safety of Tianjin University are acknowledged. The authors are also grateful for the assistance of the anonymous reviewers.

Author Contributions: Jun Zhang designed the experiments, analyzed the date and wrote the paper. Fang Liu handled the project and provided the helpful discussion. Jijian Lian made substantial contributions to conception and plan. Xiang Yan and Quanchao Ren preformed the experiments.

Conflicts of Interest: The authors declare no conflict of interest.

Abbreviations

The following abbreviations are used in this manuscript:

D	Side length of the cross section
L	Length of the prism
m_{osc}	Oscillating material mass
M_{osc}	Total oscillating mass
m_d	Displaced fluid mass
M^*	Mass ratio of the vibration system
K	System spring stiffness
ζ_{total}	Total damping ratio
$f_{n,air}$	Natural frequency in air
U	Fluid velocity
U_r	Reduced fluid velocity
A	Maximum amplitude
A^*	Maximum amplitude ratio
f_{osc}	Response frequency
f^*	Frequency ratio
V_i	Linear velocity of Gear i
V_g	Linear velocity of the generator rotor
r_i	Radius of Gear i
r_g	Radius of the generator rotor
c_i	Damping coefficient due to friction on Gear i
c_g	Damping coefficient due to friction on rotor
$\dot{\theta}_i$	Angular velocity of Gear i
$\dot{\theta}_g$	Angular velocity of the rotor
$\ddot{\theta}_i$	Angular acceleration of the ith wheel
$\ddot{\theta}_g$	Angular acceleration of the rotor
F_y	Force exerted by the fluid on the body
E	Induced voltage of the generator
B	Magnetic flux density
I	Induced current
l	Length of the wire cutting the a magnetic field
F_{mag}	Electromotive force
T_{mag}	Electromotive force torque
J_i	Rotational inertia of the ith wheel
J_g	Rotational inertia of the rotor
R_0	Generator inner resistance
R_L	load resistance
m_{equ}	Equivalent mass
c_{total}	Total system damping coefficient
$c_{structure}$	Friction damping coefficient on bearings
c_{tra}	Transmission damping coefficient
c_{gen}	Generator damping coefficient
c_{harn}	Damping coefficient due to the load resistance
P_{out}	Output power
η_{out}	Energy conversion efficiency

References

1. Blevins, R.D. *Flow-Induced Vibration*, 3rd ed.; Van Nostrand Reinhold: New York, NY, USA, 1990.
2. Williamson, C.H.K.; Govardhan, R. Vortex-induced vibrations. *Annu. Rev. Fluid Mech.* **2004**, *36*, 413–455. [CrossRef]
3. Williamsona, C.H.K.; Govardhanb, R. A brief review of recent results in vortex-induced vibrations. *J. Wind Eng. Ind. Aerodyn.* **2008**, *96*, 713–735. [CrossRef]
4. Parkinson, G.V.; Sullivan, P.P. Galloping response of towers. *J. Wind Eng. Ind. Aerodyn.* **1979**, *4*, 253–260. [CrossRef]
5. Bokaian, A.R.; Geoola, F. Hydroelastic instabilities of square cylinders. *J. Sound Vib.* **1984**, *92*, 117–141. [CrossRef]
6. Ding, L.; Zhang, L.; Wu, C.M. Flow induced motion and energy harvesting of bluff bodies with different cross sections. *Energy Convers. Manag.* **2015**, *91*, 416–426. [CrossRef]
7. Xu, F.; Ou, J.; Xiao, Y. CFD Numerical Simulation of Flow-induced Vibration with Different Cross-section Cylinders. *J. Eng. Mech.* **2009**, *26*, 7–15. (In Chinese)
8. Alonso, G.; Meseguer, J. A parametric study of the galloping stability of two dimensional triangular cross-section bodies. *J. Wind Eng. Ind. Aerodyn.* **2006**, *94*, 241–253. [CrossRef]
9. Bernitsas, M.M.; Raghavan, K.; Ben-Simon, Y. Vivace (vortex induced vibration aquatic clean energy): A new concept in generation of clean and renewable energy from fluid flow. *J. Offshore Mech. Arct. Eng. Trans. ASME* **2008**, *130*, 619–637. [CrossRef]
10. Bernitsas, M.M.; Ben-Simon, Y.; Raghavan, K. The VIVACE converter: Model tests at high damping and Reynolds number around 10^5. *J. Offshore Mech. Arct. Eng. Trans. ASME* **2009**, *131*, 403–410.
11. Chang, C.C.; Kumar, R.A.; Bernitsas, M.M. VIV and galloping of single circular cylinder with surface roughness at $3.0 \times 10^4 \leq \mathrm{Re} \leq 1.2 \times 10^5$. *Ocean Eng.* **2011**, *38*, 1713–1732. [CrossRef]
12. Park, H.; Kumar, R.A.; Bernitsas, M.M. Enhancement of flow-induced motion of rigid circular cylinder on springs by localized surface roughness at $3.0 \times 10^4 \leq \mathrm{Re} \leq 1.2 \times 10^5$. *Ocean Eng.* **2013**, *72*, 403–415. [CrossRef]
13. Ding, L. Research on Flow Induced Motion of Multiple Circular Cylinders with Passive Turbulence Control. Ph.D. Thesis, Chongqing University, Chongqing, China, 2013. (In Chinese)
14. Kluger, J.M.; Moon, F.C.; Rand, R.H. Shape optimization of a blunt body Vibro-wind galloping oscillator. *J. Fluid Struct.* **2013**, *40*, 185–200. [CrossRef]
15. Sorribes-Palmer, F.; Sanz-Andres, A. Optimization of energy extraction in transverse galloping. *J. Fluid Struct.* **2013**, *4*, 124–144. [CrossRef]
16. Luo, S.C.; Chew, Y.T.; Ng, Y.T. Hysteresis phenomenon in the galloping oscillation of a square cylinder. *J. Fluid Struct.* **2003**, *18*, 103–118. [CrossRef]
17. Ruecheweyh, H.; Hortmanns, M.; Schnakenberg, C. Vortex-excited vibrations and galloping of slender elements. *J. Wind Eng. Ind. Aerodyn.* **1996**, *65*, 347–352. [CrossRef]
18. Hmon, P.; Santi, F.; Schnoerringer, B. Influence of free stream turbulence on the movement-induced vibrations of an elongated rectangular cylinder in cross flow. *J. Wind Eng. Ind. Aerodyn.* **2011**, *89*, 1383–1395. [CrossRef]
19. Tamura, T.; Itoh, Y. Unstable aerodynamic phenomena of a rectangular cylinder with critical section. *J. Wind Eng. Ind. Aerodyn.* **1999**, *83*, 121–133. [CrossRef]
20. Li, Q.S.; Fang, J.Q.; Geary, A.P. Evaluation of 2D coupled galloping oscillations of slender structures. *Comput. Struct.* **1998**, *6*, 513–523. [CrossRef]
21. Nemes, A.; Zhao, J.; Lo Jacono, D.; Sheridan, J. The interaction between flow induced vibration mechanisms of a square cylinder with varying angles of attack. *J. Fluid Mech.* **2012**, *710*, 102–130. [CrossRef]
22. Barrero-Gil, A.; Fernandez-Arroyo, P. Maximum vortex-induced vibrations of a square prism. *Wind Struct.* **2013**, *16*, 341–354. [CrossRef]
23. Johansson, S.H.; Davidson, L.; Olsson, E. Numerical simulation of vortex shedding past triangular cylinders at high Reynolds number using a k-ε turbulence model. *Int. J. Numer. Methods Fluid* **1993**, *16*, 859–878. [CrossRef]
24. Camarri, S.; Salvetti, M.V.; Buresti, G. Large-eddy simulation of the flow around a triangular prism with moderate aspect-ratio. *J. Wind Eng. Ind. Aerodyn.* **2006**, *94*, 309–322. [CrossRef]

25. Iungo, G.V.; Buresti, G. Experimental investigation on the aerodynamic loads and wake flow features of low aspect-ratio triangular prisms at different wind directions. *J. Fluid Struct.* **2009**, *25*, 1119–1135. [CrossRef]
26. Alonso, G.; Sanz-Lobera, A.; Meseguer, J. Hysteresis phenomena in transverse galloping of triangular cross-section bodies. *J. Fluid Mech.* **2012**, *33*, 243–251. [CrossRef]
27. Alonso, G.; Meseguer, J.; Pérez-Grande, I. Galloping instabilities of two dimensional triangular cross-section bodies. *Exp. Fluids* **2005**, *38*, 789–795. [CrossRef]
28. Alonso, G.; Meseguer, J.; Pérez-Grande, I. Galloping stability of triangular cross sectional bodies: A systematic approach. *J. Wind Eng. Ind. Aerodyn.* **2007**, *95*, 928–940. [CrossRef]
29. Norberg, C. Fluctuating lift on a circular cylinder: Review and new measurements. *J. Fluids Struct.* **2003**, *17*, 57–96. [CrossRef]
30. Szepessy, S.; Bearman, P.W. Aspect Ratio and End Plate Effects on Vortex Shedding From a Circular Cylinder. *J. Fluid Mech.* **1992**, *234*, 191–218. [CrossRef]
31. Szepessy, S. On the Control of Circular Cylinder Flow by End Plates. *Eur. J. Mech. B Fluids* **1993**, *12*, 217–244.
32. Raghavan, K.; Bernitsas, M.M. Experimental investigation of Reynolds number effect on vortex induced vibration of rigid circular cylinder on elastic supports. *Ocean Eng.* **2011**, *38*, 719–731. [CrossRef]
33. Zhang, J.; Xu, G.B.; Liu, F. Experimental investigation on the flow induced vibration of an equilateral triangle prism in Water. *Appl. Ocean Res.* **2016**, *61*, 92–100. [CrossRef]